PASJ: Publ. Astron. Soc. Japan **49**, 461–470 and Plate 14 (1997)

X-Ray Analysis of the ρ Ophiuchi Dark Cloud with ASCA: Source Identification, X-Ray Spectra, and Temporal Variability

Yuichi KAMATA*
Department of Astrophysics, School of Science, Nagoya University, Furo-cho, Chikusa-ku, Nagoya 464-01
E-mail: kamata@satio.phys.nagoya-u.ac.jp

Katsuji KOYAMA† and Yohko TSUBOI
Department of Physics, Graduated School of Science, Kyoto University, Sakyo-ku, Kyoto 606-01
and
Shigeo YAMAUCHI
Faculty of Humanities and Social Sciences, Iwate University, 3-18-34 Ueda, Morioka, Iwate 020

(Received 1996 December 25; accepted 1997 May 29)

Abstract

This paper presents a comprehensive study with the Japanese X-ray astronomical satellite ASCA on X-rays from the main body of the ρ Ophiuchi dark cloud. We have constructed separate X-ray images using 3 energy bands and 12 time-sliced data, and thereby detected 19 X-ray sources, doubling the previous ASCA results of 11 X-ray sources. Three of the sources are associated with class-I infrared sources, which precede the T Tauri phase. Half of the 19 sources were found to be time variable, and 5 flare-like events with an averaged energy of $> 3 \times 10^{35}$ erg were observed. With the analogy of solar flares, we estimated the flare loop height and plasma density to be 3×10^{11} cm and 3×10^{11} cm^{-3}, respectively. Among these sources, a flare from the class-I source EL 29 exhibited an order-of-magnitude larger absorption ($N_{\rm H}$) than in quiescence states, which may indicate the exsistence of a dense protostellar disk.

Key words: Stars: flare — Stars: pre–main-sequence — Stars: X-rays — X-rays: sources — X-rays: spectra

1. Introduction

The ρ Ophiuchi dark cloud is one of the nearest well-known star-forming regions, located at $(l, b) = (353, +16)$ with a distance of 165 pc from our solar system, hence about 35 pc above the galactic plane, and extending to 10°. The total mass of the molecular gas was estimated to be $3 \times 10^4 M_\odot$, which is typical among the galactic dark clouds (Dame et al. 1987).

In the early observations of H_2CO (Loren et al. 1983), two concentrations of dense gas, named core A (near Lynds 1686) and core B (near Lynds 1681), were identified. These observations indicate peak densities of 10^5 cm^{-3} and 10^6 cm^{-3} for cores A and B, respectively. About 20 objects, including T Tauri-like variables, were found in the visual band in the vicinity of the main body. Their spectral types range from B2 V to G2 V (Chini 1981). From near-infrared observations, these cores show a high visual extinction of $A_V = 50$–100 mag (Wilking, Lada 1983; Vrba et al. 1975; Vrba et al. 1976; Chini 1981). From a $C^{18}O$ observation in this region (Wilking, Lada 1983), the size and total mass were estimated to be 1×2 pc^2 and $\sim 600 M_\odot$, respectively.

About 100 infrared objects were identified as Young Stellar Objects (YSO) in the main body of the ρ Oph dark cloud; 80% were classified into infrared classes 0 to III: 10% of class I, 50% of class II and 40% of class III objects (Andre, Montmerle 1994). From these populations of YSOs, the star-forming efficiency (SFE) was estimated to be $> 22\%$ in the ρ Oph core, which is much higher than the $> 2\%$ found in the Taurus complex (Wilking 1989).

Observations of individual objects in the infrared band have been made and discussed by many authors (Wilking et al. 1989; Elias 1978; Vrba et al. 1975; Simon et al. 1987; Adams et al. 1987; Wilking, Lada 1983; Andre, Montmerle 1994; Greene et al. 1994) and the main body is thought to be a progenitor of a bound open cluster, while the Taurus complex is thought to produce field stars.

The class-0 sources are the gravitational collapsing phase in molecular cores, growing central condensation with gas infall onto large circumstellar disks. In the next

* Present address: Research Center for Advanced Energy Conversion, Nagoya University, Furo-cho, Chikusa-ku, Nagoya 464-01.

† Also CREST, Japan Science and Technology Corporation (JST), 2-1-6 Sengen, Tukuba-shi, Ibaraki 305.

stage, the class I-phase, gas accretes from the disk onto the central object, which may be called protostars. The following stages have been observationally and theoretically well studied, characterized by a quasi-static evolution and are called "Classical T Tauri Stars" (CTTS) and "Weak Lined T Tauri Stars" (WTTS), roughly corresponds to class-II and -III, respectively (for reviews, see Shu et al. 1987; Wilking 1989).

The Einstein satellite found that class-II and -III sources are bright and variable in the soft X-ray region (Montmerle et al. 1983). Their X-ray spectra can be fitted by a thin thermal model with a temperature of about 1 keV, suffering absorption column densities in the range 10^{20}–10^{21} cm^{-2}. These X-ray sources show flickering in the soft X-ray band, referred to as an *X-ray Christmas Tree*. The overall distribution of the normalized amplitude variations are reproduced by a power law with an index of 1.4, which is similar to that of solar flares (Montmerle et al. 1983). Thus, the flickering phenomenon was explained by solar-like flare activities. No X-rays were found from any class-I sources. Casanova et al. (1995), with the recent deep ROSAT observation, reported 55 reliable detections of X-ray sources in the 1.0–2.4 keV energy band. Seven class-I sources lie within the error circles of X-ray peaks. Then, X-rays from one of the class-I sources was confirmed with the following HRI observation (Grosso et al. 1997). Neither Einstein satellite nor ROSAT detected X-rays from the class-0 source VLA 1623.

The hard X-ray band (> 4 keV), on the other hand, has been studied by non-imaging instruments; hence, only spatially averaged information of each molecular core with a typical size of a square degree was available. The hard X-ray spectra of star-forming regions obtained by the Japanese X-ray satellites Tenma and Ginga showed a higher temperature of $kT \sim 4$ keV with $N_{\rm H} \sim 10^{22}$ cm^{-2} and a Fe abundance of 0.3–0.4 cosmic (Koyama 1987; Koyama et al. 1992). The temperature determined with hard X-rays was significantly higher than that found in the soft X-rays as well as those of typical solar flares, thus increasing the controversy on the X-ray origin from the dark cloud. Another unsolved question is whether or not class-0 and -I sources are X-ray emitters.

These issues are now being largely addressed by the ASCA wide-energy band observations. In an early report, Koyama et al. (1994 ; hereafter Paper I) found several hard X-ray sources in the core region, which were not seen in the Einstein IPC band pass of 0.3–4 keV. These sources are deeply embedded objects with an equivalent hydrogen-column density of 10^{22} cm^{-2}.

Following Paper I, we have made a further source finding and identification using 3 energy bands and 12 time-sliced images, and performed spectral and timing studies for these sources. We present here a comprehensive report on the ASCA X-rays from the ρ Oph dark cloud. Throughout this paper we assume the distance to the ρ Oph core to be 165 pc (Dame et al. 1987).

2. Observation and Source Selection

The ASCA observations were made with two sets of solid state imaging spectrometers (SIS) and gas imaging spectrometers (GIS) as focal-plane instruments of four X-ray telescopes (XRT). The nominal energy range of these instruments is 0.5–10 keV with an effective area for each XRT of 300 cm^2 and 200 cm^2 at 1.5 keV and 4.5 keV, respectively (Burke et al. 1991; Tanaka et al. 1994; Serlemitsos et al. 1995; Tsusaka et al. 1995; Ohashi et al. 1996). The field of view of the XRT is about 30′ in diameter (FWHM), while the GIS and SIS cover about 40′ diameter and 22′×22′ of the sky, respectively. The ASCA satellite was pointed at the central position of the ρ Oph dark-cloud main body, $(\alpha, \delta)_{\rm J2000} = (16^{\rm h}26.^{\rm m}8, -24°31')$ for about a 40 ks effective exposure during a time span of 70 ks, starting from 02:19 to 22:45 on 1993 August 20. Since the systematic error of ASCA positions can be as large as about 1′, we refined the sky coordinates of the ASCA image by referring to the ROSAT position of ROXR1-13, $(16^{\rm h}26^{\rm m}3.^{\rm s}2, -24°23'36'')_{\rm J2000}$. We searched for X-ray peaks in the 1–2 keV, 2–5 keV, and 5–7 keV energy bands. In addition, we made 12 time-sequentially sliced images in both the 0.5–2 keV and the 2–10 keV energy bands. The typical exposures and time span of each image were 3 ks and 1.5 hr, respectively. These images were also used to study the temporal variability. As we note later, we found X-ray flares with typically a few hours of decay time. We therefore could efficiently search for variable sources using these time-sliced images with a rather enhanced signal-to-noise ratio compared to the time-averaged image of full exposure.

Source detection is not a simple process, due to the position-dependent point-spread function of the XRT (blurring and aberration; Serlemitsos et al. 1995; Tsusaka et al. 1995), shaded by the window supporting grid of GIS, the dead regions between CCD chips and the contamination of nearby bright sources. Furthermore, these complicated effects are energy dependent.

Thus, for simplicity, we uniformly set 3 criteria for the source detection. The first is:

1. The threshold level was set at S/N = 5 (0.5–10 keV) using photons within a radius of 0.′5, which includes 16% of the incident flux.

The X-ray peak profiles of the GIS instruments were greatly smeared compared to the sharp peak of XRT (Tsusaka et al. 1995; Serlemitsos et al. 1995), and the GIS has a typical energy-dependent positional accuracy of 0.′5 at 6 keV (Ohashi et al. 1996). We therefore adopted a positional error of 0.′5. On the other hand, since no smear effect was found in the SIS image, the position error is as small as about 0.′25. Accordingly, we set a second

criterion of the source detection:
2. We required simultaneous detection of GIS 2 and GIS 3 within 0.′5, or SIS 0 and SIS 1 within 0.′25, or both.
We found that bright sources often make spurious peaks on the *Maltese Cross* shape of the XRT response function (Tsusaka et al. 1995). We therefore generally excluded these possible ghost peaks with the following criterion:
3. We ignore the instrumental peaks found near to bright X-ray sources.
The most severe condition was found to be the 2nd item. After screening with these criteria, we selected 19 X-ray peaks from the 108 X-ray images.

3. Results and Discussion

3.1. Source Identifications

In addition to the sources found in Paper I, X-ray sources, designated as C1–C7, were found in various energy bands. Sources C2 and C5 were identified during their flare phase (both were found in the period 21:16–22:13 on 1993 August 20) in the 2–10 keV energy band image. We also resolved source No. 9 (in Paper I) into 9A and 9B using the soft- and hard-energy band images.

To extract the source counts, an aspect correction of X-ray telescope was made using a ray-tracing simulation program (Tsusaka et al. 1995) assuming monochromatic incident X-rays of 1.5 keV, 3.0 keV, and 6.0 keV for the 1–2 keV, 2–5 keV, and 5–7 keV band data, respectively. We also subtracted blank-sky data, which included the internal background and the Cosmic X-ray Background (CXB) for both the GIS and SIS data. The internal background levels were below 10% of typical X-ray sources, and the CXB level was also at the same level; thus any possible error due to background subtraction is negligibly small. The results of the detected point sources and their X-ray fluxes in the 3 energy bands are summarized in table 1. Optical or IR counterparts were simply selected from the currently available catalog (see table notes). The counterparts lying within 0.′25 of SIS sources were assigned high confidence (Level 1 in the table), while those within 0.′5 of GIS sources were assigned a lower confidence (Level 2). Compared to the Einstein and ROSAT images, we discovered eight (No.'s 6, 8, 9B, 10, C1, C2, C5, C7) new X-ray sources. A new source (No. C2) is neither an optical nor IR candidates in the error region.

3.2. X-Rays from Class-0 and -I Candidates

To demonstrate the higher capability of the present source finding procedure than that reported in Paper I, we show two energy-band SIS images (combined images of SIS 0 and 1), together with a molecular-cloud contour map and catalogued infrared sources around the molecular core and RGB (red, 5–7 keV; green, 2–5 keV; blue, 1–2 keV) weighted GIS (GIS 2 and 3 combined) and SIS (SIS 0 and 1 combined) images of the entire field of view in figure 1 (Plate 14) . We see point sources near to the cloud core only in the hard X-ray band. Remarkably, we found X-rays from two (EL 29 and WL 6) and possibly one more (WLY 2–46) class-I source. No class-I sources were found using the soft-band Einstein telescope (Montmerle et al. 1983), while Casanova et al. (1995) reported the possible detection of 7 class-I candidates (GSS 30–IRS 1/LFAM 1, GY 224, WL 6/GY 256, IRS 43, IRS 44/IRS 46, IRS 54, and IRS 48) with the ROSAT telescope. They noted, however, that these class-I identifications are marginal due to source confusion in the crowded region. One may argue that the source-confusion problem is not improved with the ASCA observations because of the rather limited spatial resolution (about 3′ of the half-power diameter) of XRT compared to ROSAT. However, the response function of XRT has a cusp-shape structure with a sharp peak at the image center. We can thus separate, for example, two point sources with a separation angle less than 0.′5 using the peak position of the SIS images [see figure 1 (Plate 14)]. In particular, X-ray detection from class-I sources EL 29 and WL 6 is very certain, because no other candidate exists in the X-ray error region. Recently, Grosso et al. (1997) confirmed the X-ray emission from the class-I source IRS 43 with a deep exposure of the HRI image. Koyama et al. (1996) found hard X-rays from a cluster of class-I objects at the core of the R CrA molecular cloud. Accordingly, the present paper would be the third report for the highly possible detection of X-rays from class-I objects. Further detailed discussions on individual class-I sources are given separately in subsection 3.6. No X-rays were found from the GIS and SIS positions of the class-0 source VLA 1623.

3.3. Variabilitiy and Flares

To estimate temporal variations of individual X-ray sources, we examined source intensities in the 0.5–2 keV and 2–10 keV energy band during 12 different epochs for each source, with a typical exposure and time span of 3 ks and 1.5 hr, respectively. We applied the Kolmogorov-Smirnov test under the assumption of constant flux for individual sources using the XANADU/XRONOS (Ver. 4.02) software package. The thus-obtained variability probabilities are given in table 2 together with the maximum and minimum luminosities in the 2–10 keV energy bands. From the table, we can see that about one third of the sources show significant variability during an observation time span of around 70 ks. For a comparison, we also list the Einstein results for variability.

Among the variable sources, 5 flare-like events were found, as noted in table 2. An example of the flare profile, the light curve of a flare from the No. 2 source, is given

Table 1. Summary of identifications.

No. ROXA	$(\alpha, \delta)_{J2000}$	1–2 keV [count s^{-1} cm^{-2} $\times 10^{-5}$]	2–5 keV	5–7 keV	$\log(L_x)$ [erg s^{-1}]	S/N[!]	Level[*]	Class (IR)	V/A_V/Sp[$]	K mag[%]	ID[+]
1	($16^h25^m51.2^s$, $-24°39'06''$)	4.6±0.5	6.9±0.7	1.8±0.5	30.8	14.7	2		15.3/5.9/K2	8.3	ROX4=ROXs4=ROXR1–8=VSS23=WLY2–10
2	($16^h25^m57.7^s$, $-24°30'35''$)	3.6±0.3	4.4±0.5	1.8±0.4	30.8	14.4	1	III	16.9/4.7/K7	8.29	ROX7=ROXs7=ROXR1–10=GSS20=WLY1–24=WLY2–13
3	($16^h26^m03.2^s$, $-24°23'36''$)	23.8±0.9	26.5±1.2	9.6±0.9	31.4	41.7	...	IIID	13.9/6.6/K0	6.13–6.22	ROX8=ROXs8=ROXR1–13=HBC637=EL14=Haro1–6=ROC8=ROS4=GSS23 =WLY1–26=VSS93=DoAr21=SFAM7=C10=SHO22
4	($16^h26^m23.2^s$, $-24°21'03''$)	3.3±0.3	3.8±0.4	1.4±0.3	30.6	14.1	1	II	14.6/6.6/K0	6.17–6.85	ROXs10B=EL22=HBC639=GSS31=C16=WSB30=DoAr24E=SKS162322.0−241415 =GY20
5	($16^h26^m34.4^s$, $-24°23'28''$)	1.3±0.2	2.1±0.3	1.1±0.2	30.7	11.5	2	IIID	19.00/11.7/B5 V	6.29–7.52	ROX14=ROXs14=ROXR1–28=EL25=VSS26=ROC15=ROS8=LFAM11=GSS35 =WLY1–36=S1=SFAM13=C19=BZ Oph4=SKS162332.8−241645=CRB2332.6−1640=GY70
6	($16^h27^m02.8^s$, $-24°44'56''$)	1.4±0.3	2.4±0.4	1.2±0.4	30.4	8.9	2				GY186
7	($16^h27^m09.3^s$, $-24°34'11''$)	0.5±0.1	1.7±0.3	1.0±0.2	30.6	10.7	1	II		8.75–8.92	ROXR1–37=WL10=BBRCG24=CRB2407.3−2735=GY211
8	($16^h27^m09.3^s$, $-24°37'27''$)	0.2±0.1	1.7±0.3	2.6±0.4	31.0	8.4	1	I		6.78–8.18	EL29=LFAM27=WL15=ROXC15=WLY1–7=BBRCG23=SKS162407.9−243037 =CRB2407.8−3033=GY214
9A	($16^h27^m19.8^s$, $-24°41'35'$)	1.7±0.3	2.3±0.4	1.5±0.4	30.5	14.6	1	III	13.4/0.6/K4+M2.5	8.46–9.10	ROX21=ROXs21=ROXR1–41=HBC263=SR12=NSV7725=WLY1–13 =WLY2–40=SKS162417.8−243459=CRB2417.6−3500=GY250
9B	($16^h27^m30.0^s$, $-24°39'42'$)	1.1±0.2	3.4±0.5	1.6±0.4	30.7	10.1	2	(I)		9.70–10.59	WLY1–16=WLY2–46=BBRCG52=SKS162427.7−243235=GY274 /GY282
10	($16^h27^m21.7^s$, $-24°29'57''$)	0.9±0.2	3.3±0.4	1.7±0.3	30.9	12.2	1	I		9.93–10.04	WL6=WLY1–14=BBRCG38=SKS162420.2−242312=CRB2420.4−2307=GY254
11	($16^h27^m41.5^s$, $-24°21'59''$)	3.1±0.4	1.7±0.4	0.9±0.3	30.0	10.3	2	(II)	11.5/0.2/K4+K6	7.0–7.57	ROX29=ROXs29=ROXR1–52=NSV7733=HBC264=SR9=EL34=WSB54 =CD−24−12689=AS207=WLY1–49=WLY2–52=DoAr34=GY319=C29 /GY327
C1	($16^h25^m25.0^s$, $-24°27'07''$)	1.3±0.3	1.1±0.3	0.4±0.2	29.9	6.7	2				SHO18
C2	($16^h26^m02.7^s$, $-24°31'38''$)	2.3±0.3	3.3±0.4	1.3±0.3	30.6	11.6	1				none
C3	($16^h26^m24.5^s$, $-24°24'54''$)	1.2±0.2	2.6±0.3	1.4±0.3	30.8	10.5	1	(II)		7.02–7.08	ROXR1–25=ROXC6=EL23=GSS32=S2=SKS162322.6−241803=GY23 =CRB2322.6−1802
										10.90–10.91	/GY29=CRB2323.8−1801=SKS162323.8−241800
C4	($16^h26^m44.0^s$, $-24°20'48''$)	1.4±0.2	1.6±0.3	0.5±0.2	30.4	11.9	2	II		7.94–8.05	ROX15=ROXR1–29=GY110=EL26=VSSG2=GSS37
C5	($16^h27^m06.4^s$, $-24°38'09''$)	0.2±0.1	0.9±0.2	1.5±0.3	30.4	8.1	1	(II)		10.40–11.30	WL17=GY205=BBRCG22=SKS162405.3−243133=CRB2404.8−3133 /GY201
C6	($16^h27^m18.9^s$, $-24°29'00''$)	0.8±0.1	3.3±0.4	1.3±0.3	30.9	11.6	1	II		9.20–9.63	VSSG26=WLY1–12=WLY2–39=WL4=BBRCG40=CRB2417.0−2221=GY247 =SKS162417.0−242225 /ROX22=ROXR1–40
C7	(16h27m21.2s, $-24°43'40''$)	1.4±0.3	2.5±0.5	1.3±0.4	30.3	8.2	2			10.87–11.54	GY253=SKS162420.0−243654

[*] Detection and candidate level 1: within 0.′25 error radius for SIS and 2: within 0.′5 error radius for GIS.
[!] S/N due to photon statistics within 0.′5 error circle in the 0.5–10 keV energy band (SIS: level 1, GIS: level 2).
[$] Visual magnitude, visual extinction, and spectral type of visible sources
[%] K band magnitude (divergences indicate the minimum and the miximum value of the different references)
[+] Abbreviations are AS (Merrill, Burwell 1950), BBRCG (Barsony et al. 1989), BZ (Brown, Zuckerman 1975), C (Chini 1981),CD (Thome 1892), CRB (Comeron et al. 1993), DoAr (Dolidze, Arakelyan 1959), EL (Elias 1978), GSS (Grasdalen et al. 1973), GY (Greene, Young 1992), Haro-1 (Haro 1949), HBC (Herbig, Bell 1988), LFAM (Leous et al. 1991), NSV (Kukarkin et al. 1981), ROC/ROS (Andreet al. 1987), ROX (Montmerle et al. 1983), ROXs (Bouvier, Appenzeller 1992), ROXR1 (Casanova et al. 1995), S (Vrba et al. 1975), SFAM (Stine et al. 1988), SHO (Schlickeiser et al. 1989), SKS (Strom et al. 1995), SR (Struve, Rudkjøbing 1945), VSS (Vrba et al. 1976), VSSG (Vrba et al. 1975), WL (Wilking, Lada 1983), WLY 1 (table 1 in Wilking et al. 1989), WLY 2 (table 2 in Wilking et al. 1989), WSB (Wilking et al. 1987).

Table 2. The minimum and maximum luminosities and flare events.

No. ROXA*	$L_{x_{max}}$ (2–10 keV) [$\times 10^{30}$ erg s^{-1}]	$L_{x_{min}}$ (2–10 keV) [$\times 10^{30}$ erg s^{-1}]	Variability propability† (0.7–10 keV)	ASCA Flare	IPC‡ Variability
1	7.3± 2.3	1.6± 1.5	99.4%		yes
2	22.9± 4.2	0.7± 0.7	>99.9%	yes	yes
3	38.5± 6.9	23.6± 3.7	73.7%		yes
4	9.0± 2.3	2.3± 1.2	80.6%	yes	
5	6.6± 2.1	1.9± 1.7	47.3%		yes
6	5.9± 2.0	<2.4	69.3%		
7	11.0± 4.3	1.1± 1.1	>99.9%	yes	
8	54.1± 9.9	3.3± 2.3	>99.9%	yes	
9A	4.6± 1.9	1.6± 1.1	53.7%		yes
9B	10.5± 4.4	2.5± 1.5	90.8%		
10	13.9± 5.1	2.5± 1.7	>99.9%		
11	2.3± 1.0	0.5± 0.5	50.8%		
C1	1.9± 1.1	<2.4	40.5%		
C3	9.3± 2.2	3.6± 1.6	83.8%		
C4	5.6± 2.1	1.0± 0.8	93.2%		yes
C7	7.1± 2.4	1.0± 0.8	96.2%	yes	

* Sources No. C2, C5, and C6 are ignored because of contamination of nearby bright sources.
† Variability probability of X-ray flux in the 0.7–10 keV with Kolmogorov-Smirnov test using XANADU/XRONOS version 4.02.
‡ X-ray variability in the 0.3–4 keV energy band of Einstein IPC observation (Montmerle et al. 1983).

in figure 2, in the soft and hard X-ray bands together with the hardness ratio. We can clearly see fast rises and a slow exponential decays in both the flux and hardness ratio; similar features found in the flare from class-II or -III objects (T Tauri stars). Class-I flares have also been reported from IRS 43 in Ophiuchus (Grosso et al. 1997) and R CrA (Koyama et al. 1996).

From the light curves of the five flares, we estimated exponential decay times are around 7–32 ks and the total 2–10 keV energies are around (2–6) $\times 10^{35}$ erg. Since the decrease in the hardness ratio is attributable to a decrease of the plasma temperature, we could estimate the plasma density from the decay time beyond on the assumption of radiative cooling of a thin thermal plasma. We also estimated the flare loop height (assuming a single-loop) based on the analogy of a solar flare (van den Oord 1988) with $\alpha = 0.1$ (ratio between the diameter and length of the loop) and $\Gamma = 2$ (ratio of the cross sections between the loop top and bottom). Due to the limited photon statistics of the X-ray flare, we fixed the peak temperature to be 7 keV, the best-fit value for the case of the No. 2 flare. The thus-derived physical parameters have a large error. Nevertheless, for a semi-quantitative discussion and a comparison for other flare data, we list the best-fit values in table 3. Typical values of the electron density and flare loop height are 3×10^{11} cm^{-3} and 3×10^{11} cm, respectively. Since 1/4 of all the X-ray sources show X-ray flares of $E_x > 10^{35}$ erg, we can estimate the frequency of such a large flare as being one flare per 4 days. Assuming equilibrium between the thermal pressure and magnetic field pressure, we crudely estimated the magnetic field strengths of the X-ray emitting plasma to be 200–400 Gauss.

3.4. *X-Ray Spectra of the Cloud Cores*

In order to study the global spectral structure of the cloud, we also obtained wide-region GIS spectra from Lynds 1686 and Lynds 1681, with 6′ and 9′ radii from their C^{18}O intensity peaks of $(16^h26.^m3, -24°22')_{J2000}$ and $(16^h27.^m1, -24°35')_{J2000}$, respectively. The background spectra were taken from the off-plane blank-sky field. We fitted it to a single-temperature thin-thermal model (Raymond-Smith model, or R-S in short; Raymond, Smith 1977) with the absorption-column density N_H (Morrison, McCammon 1983). We referred to the metal abundance table by Feldman (1992) for the R-S model to these background-subtracted spectra. For simplicity, we assumed a point source for the aspect response function generated in several energy bands, because the reflectivity of the X-ray telescopes depends on the incident X-ray energy (Tsusaka et al. 1995). All of the spectra were well explained by R-S models with the best-fit parameters listed in table 4. All of the errors of the parameters obtained from spectral fitting were 90%

Table 3. Summary of flare parameters.

No. ROXA	e-fold [hr]	log ($L_{x_{max}}$) [erg s^{-1}; 2–10 keV]	log (E_x) [erg; 2–10 keV]	log (n_e) [cm^{-3}]	log (H) [cm]	log (B) [G]
2.....	1.7	31.4	35.1	11.5	11.1	2.6
4.....	4.3	31.0	35.1	11.1	11.7	2.4
7.....	10.8	31.0	35.6	11.7	11.6	2.2
8.....	2.3	31.7	35.7	11.3	11.4	2.5
C7.....	2.6	31.0	35.0	11.3	11.1	2.5

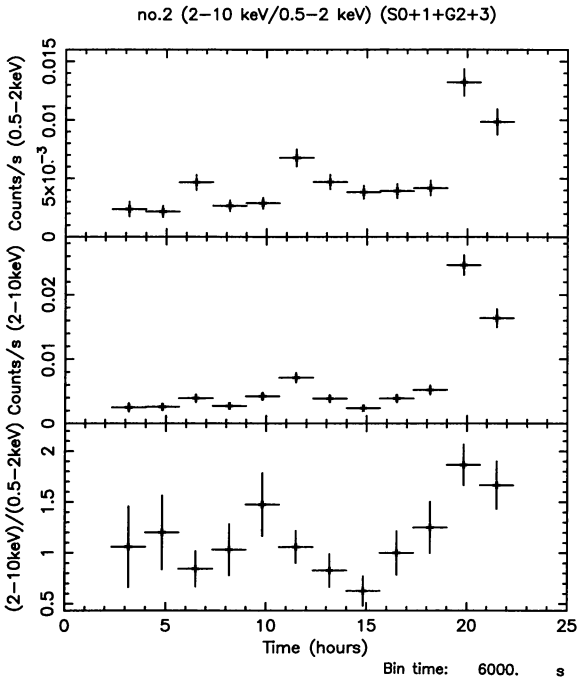

Fig. 2. Light curves of source No. 2 in the 0.5–2 keV band (upper panel) and 2–10 keV band (middle panel). The data are the summed count rate of SIS 0+1 + GIS 2+3 within 1′.5 radius. The ratio of the hard bands to the soft band (the hardness ratio is given in the lower panel. The horizontal axis shows the epoch from 1993 August 20 0:00. The minimum and maximum of the hardness ratio correspond to temperatures of 2 keV and 7 keV, respectively.

confidence errors, unless otherwise mentioned.

The spectra of the cloud core regions show higher temperatures of 4.7 and 2.7 keV for near L1681 and L1686, respectively, than the commonly accepted temperature of the star-forming region of about 1 keV (Montmerle et al. 1983). The best-fit abundance of these cloud cores are found to be about 0.3 cosmic. Since the spectrum of Lynds 1686 is dominated by the brightest X-ray source, No. 3 (ROX-8) in the field of view, we made two temperature model fittings with fixed parameters for the No. 3 source, which was determined separately, and varied another set of R-S parameters. The best-fit temperature was then increased to be 4.6 keV (table 4).

By inspecting the catalogued IR source distribution (Wilking et al. 1989), we found that the L1686 region is dominated by class-II and -III sources, while the catalogued IR sources are rather sparse in the L1681 region. Also, the distribution of soft X-ray sources, e.g., the ROSAT observation, shows more sources in the L1686 than in the L1681 regions. We therefore infer that the L1681 region is more crowded with deeply embedded sources than in L1686. It would be reasonable to assume that possible embedded sources in L1681 are dominated by a younger stage (class-I, for example) than those of the catalogued sources (mostly class-II and -III) found in L1686. Since the X-ray temperatures of the two clouds are essentially indistinguishable, no spectral dependence on the evolutionary stage is inferred. This is in sharp contrast to the R CrA cloud, in which class-I sources definitely show a higher temperature than the surrounding class-II and -III objects (Koyama et al. 1996). To study whether or not class-I objects, as a whole, exhibit a higher temperature than class-II or -III would be an important subject for future X-ray astronomy. We also note that the plasma temperature of 3–4 keV and abundance of 0.3 cosmic found in the cloud cores are entirely consistent with the results of the non-imaging instruments of Ginga and Tenma (Koyama 1987).

3.5. X-Ray Spectra of Individual Sources

The GIS and SIS spectra of relatively bright and isolated sources were analyzed after the background subtraction outlined in subsection 3.4. For these individual sources, we made a combined fitting of the SIS and GIS spectra, unless otherwise noted. The elemental abundance was a free parameter for the stronger sources (2, 3, 8, and 10), but was fixed at 0.3 cosmic for fainter sources, consistent with the global abundance found above. We also note that the abundances of No. 2, No. 3, and No. 8 in quiescence show values consistent with 0.3 cosmic.

As noted in subsection 3.2, some sources show either flare activities or a large time variability; we analyzed

Table 4. The best-fit spectral parameters.

No. ROXA	Instrument	kT^* [keV]	$N_{\rm H}^*$ [$\times 10^{22}$ cm^{-2}]	Fe abundance* (ratio to the cosmic)	Redχ^2 (d.o.f.)	Comment†
1	GIS	2.23+1.42/−0.61	0.84+0.35/−0.33	0.3 fixed	1.25 (82)	
2	GIS&SIS	2.64+0.54/−0.40	0.83±0.13	<0.32	1.07 (115)	
2	GIS&SIS	2.89+0.54/−0.51	1.08+0.26/−0.23	0.94+1.32/−0.65	1.08 (47)	Flare
2	GIS&SIS	1.35+0.56/−0.35	0.93+0.45/−0.26	<0.37	1.43 (16)	Quiescent
3	GIS&SIS	2.37+0.12/−0.14	1.03+0.07/−0.05	0.25±0.10	1.07 (217)	
8	GIS&SIS	11.3+17.8/−5.0	9.5+2.9/−2.3	1.6+∞/−0.9	1.42 (53)	
8	GIS&SIS	4.0+4.6/−2.3	19+11/−6	1.2+2.6/−0.6	1.94 (53)	Flare
8	GIS&SIS	3.0 fixed	3.8+1.5/−1.3	0.37+1.19/−0.37	1.94 (53)	Quiescent
9A	SIS	0.73±0.16	0.7+0.2/−0.3	0.3 fixed	1.42 (9)	
9B	GIS	4.1+4.3/−1.1	2.8±1.1	0.3 fixed	1.05 (40)	No. 9A and 9B‡
10	GIS&SIS	3.2+0.9/−0.7	4.1+0.7/−0.6	<0.21	1.01 (56)	
10	GIS&SIS	2.2+0.5/−0.4	4.6+1.0/−0.6	0.3 fixed	1.55 (56)	High state
10	GIS&SIS	2.2+1.0/−0.6	5.0+1.4/−1.1	0.3 fixed	0.88 (53)	Low state
11	GIS	0.73+0.29/−0.15	0.36+0.22/−0.36	0.3 fixed	1.11 (19)	
L1686	GIS	2.74+0.16/−0.14	1.09±0.07	0.29±0.12	1.29 (180)	r<6′
L1686	GIS	4.6+4.0/−1.5	1.6+1.7/−0.6	0.3 fixed	1.30 (180)	L1686&No.3‡
L1681	GIS	4.74+0.97/−0.68	2.73+0.28/−0.26	0.39+0.13/−0.12	1.04 (159)	r<9′

* Data without errors are fixed parameters. Errors and upper limits are 90% confidence level.
† Comments are for flare or quiescent component and high or low state.
‡ No. 9A and 9B or L1686 and No. 3; combined fitting (see text).

separately the flare and quiescent spectra (in the case of No. 2 and 8), or the spectra during high (higher than averaged flux) and low(lower than averaged flux) states (in case of No. 10), and attempted R-S model fitting. For the flare spectra, we subtracted the quiescent data, while the background spectra for the quiescent data are the same, as mentioned regarding the overall source spectra (blank-sky data).

In addition to these spectral analyses, we estimated the overall X-ray properties of the detected X-ray sources using the three band (1–2 keV, 2–5 keV, and 5–7 keV) fluxes (see table 1). The results are given in figure 3 by a two-color diagram. From this figure we found that the temperature and absorption of most sources ranged between 2–5 keV and (1–5)$\times 10^{22}$ cm^{-2}, respectively. These are consistent with the results from a spectral fitting of the individual sources shown in table 4. Adopting these spectral parameters, we calculated the total X-ray luminosities listed in table 1. The luminosity in the 2–10 keV band ranges from $10^{29.9}$ to $10^{31.4}$erg s^{-1}, which is roughly the same as that found in the lower energy band of 0.4–4 keV (e.g., Montmerle et al. 1983). Thus, the X-ray luminosity from YSOs, at least those in the ρ Oph cloud, is approximately equal in the soft and hard X-ray bands.

Since those sources associated with the class-I counterparts exhibit a larger absorption in X-rays than do class-II or -III objects (see table 4), we compared the $N_{\rm H}$ and $H-K$ obtained by the X-ray and near-infrared observations. In table 5 we have listed the previously reported $H-K$ magnitude and the ratio between $H-K$ and $N_{\rm H}$ (X-rays).

The A_V values of the class-IIIs are almost consistent with the galactic gas-to-dust mass ratio of $\sim$ 200 (Gorenstein 1975; Ryter et al. 1975; for review, see Ryter 1996), while those of class-Is are equivalent to 3-times smaller values, assuming a black-body temperature of 3500 K for the central stars (e.g., Kenyon et al. 1993a) and the dust-size population from Savage and Mathis (1979). Such a large fraction of dust compared to gas cannot be easily understood, because even if all heavy elements are depleted into dust grains, a factor of 3 enrichment of dust can, at most, be obtained (Sofia et al. 1994). In class-Is and -II with stellar disks, the X-ray emitting region would be more deeply inside than the infrared-emitting region; the X-rays are more absorbed than the infrared. Thus, the small $N_{\rm H}/H-K$ ratios of class-Is compared with class-IIIs are hardly understood; they possibly require a particular geometry or lower star temeperature than expected.

For detailed modelings, we certainly need more studies as to whether or not such lower $N_{\rm H}/H-K$ ratios in class-Is are common in star-forming regions (e.g., Kenyon et al. 1993a, 1993b), which is beyond the scope of this paper.

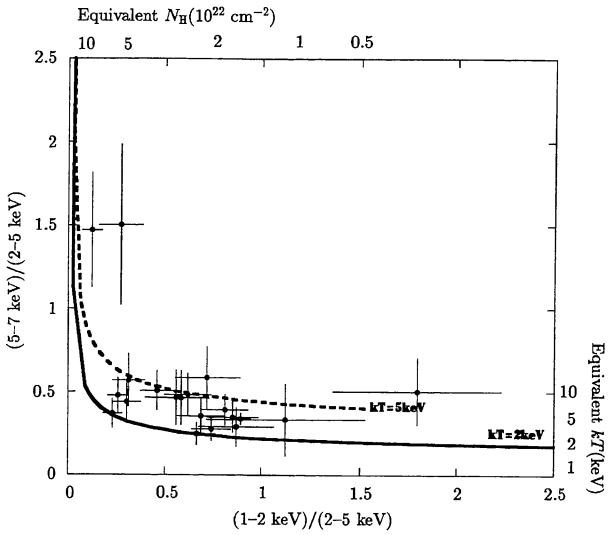

Fig. 3. X-ray color-color diagram for the detected sources (see table 1). The horizontal axis shows the count ratios in the 1–2 keV and 2–5 keV bands, while the vertical axis is for the ratios between 2–5 keV and 5–7 keV bands. The solid and dotted curves are predicted iso-temperature curves of a thin thermal model (R-S model).

3.6. *Comments on Selected Sources*

No. 2

Source No. 2 was identified as being ROX-7; which showed temporal variability by factor of 2 in the Einstein IPC observations with a maximum time scale of < 2 d. During the ASCA observation, this source showed an X-ray flare (figure 2). The temporal variation of the hardness ratio corresponds to a temperature variation from 2 to 7 keV, assuming a constant N_H of 1×10^{22} cm^{-2}. The spectral analysis during the flare and quiescent were separately carried out with the best-fit parameters listed in table 4. We found that the flare temperature was significantly higher than the quiescent value. The mean flare temperature of about 3 keV is almost same as the results from non-imaging X-ray observations of Ginga and Tenma (Koyama 1987; Koyama et al. 1992) and the averaged spectra of the ρ Oph cloud cores with ASCA.

No. 3

The source is the brightest source in the field, one order of magnitude brighter than any other source, and is thus chosen for a boresight determination (section 2). No variability was found. A detailed spectral analysis using the SIS instrument was already presented in Paper I.

Table 5. X-ray and infrared characteristics.

No. ROXA	IR* class	$H-K$(ref)† [mag]	$N_H/H-K$‡ [$\times 10^{22}$cm^{-2}mag^{-1}]
2.....	III	0.56±0.04(WLY2)	1.7(1.2–2.5)
3.....	IIID	0.64±0.14(EL)	1.6(1.5–1.7)
8.....	I	4.01±0.04(SKS)	0.9(0.6–1.3)
9B	I	3.14±0.05(SKS)	0.9(0.5–1.2)
10.....	I	4.01±0.09(SKS)	1.2(1.0–1.6)
11.....	II	0.60±0.14(EL)	0.6(0.0–1.0)

* IR class: Andre and Montmerle (1994).
† $H-K$ values: abbreviations are the same as table 1.
‡ uncertainties in the brackets are due to N_H error in table 4.

No. 7

In Paper I, this source is identified as an IR source, either GY 211, WL 10, or GY 220, but have now been firmly identified as being WL 10. This source showed a significant time variability in both the soft (0.5–2 keV) and hard (2–10 keV) bands. The equivalent temperature and absorption of this source are 2 keV and 4×10^{22} cm^{-2}, respectively. This result indicates the class-I nature of this object.

No. 8

We found only one IR candidate (EL 29) in the error region of source No. 8. We can thus firmly identify this source as being EL 29, an infrared variable (Elias 1978), class-I object located near to the CO peak (Wilking, Lada 1983) near Lynds 1681. A hard X-ray flare in the 2–10 keV energy band was found with the parameters listed in table 2. More detailed comparisons of the flare and the quiescent states are given in table 4. We note that the flare spectrum showed significantly higher absorption of about $N_H = 2 \times 10^{23}$ cm^{-2} than that found in the quiescent spectrum ($N_H = 4 \times 10^{22}$ cm^{-2}). EL 29 shows a deep silicate absorption feature (Hanner et al. 1995), which indicates an edge-on geometry of the circumstellar disk (e.g., Kenyon et al. 1993a). Simon (1987) found that the circumstellar envelope has a spatial extent of 10^2 AU. We therefore infer that the excess absorption during the X-ray flare arises through the dense disk along the line of sight, while the quiescent X-rays are produced over the region of the stellar surface, which do not suffer disk extinction.

No. 9B

This source is clearly found in the hard (2–10 keV) energy band near the position of No. 9 (Paper I). Two IR candidates, GY 282 and a class-I object, WLY 2-46, are within the error circle.

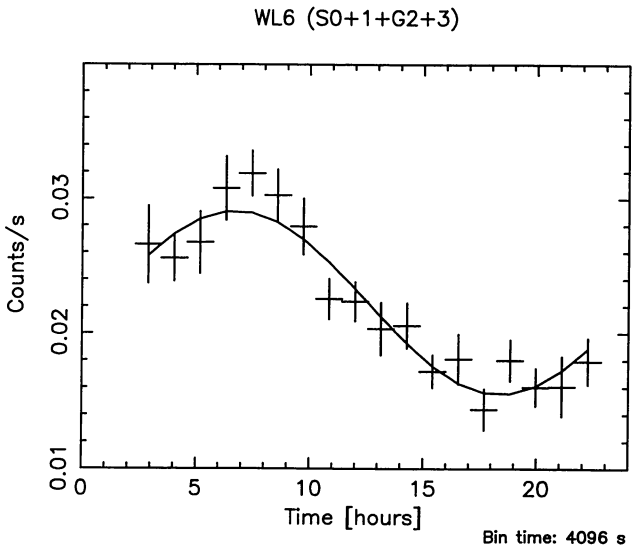

Fig. 4. X-ray light curve of source No. 10 in the 0.5–10 keV energy band. The vertical axis shows the SIS 0+1 + GIS 2+3 counts within 3′ radius [counts s^{-1}]. The horizontal axis shows the time [hr] from 1993 August 20 0:00. The period is about 0.97 d with an amplitude of 30%.

No. 10

Only one young stellar object, the class-I source WL 6, lies within the error circle of the source. It exhibited sinusoidal variability during the observation (figure 4). No significant difference in the plasma temperature and absorption between the high- and low-state spectra was found (table 4). These characteristics differ from the flare properties of other sources. We suspect that the energy-independent and sinusoidal modulation of No. 10 is due to stellar rotation with a period of about 0.97 d, with a large sunspot or coronal hole covering about 30% of the stellar surface. Near-infrared observations show that fast rotation periods and large sunspots are general characteristics of many T Tauri stars (Hartmann et al. 1987). Also, fast stellar rotation causes a high X-ray luminosity, as in RS CVn stars (Rosner et al. 1985). If the flux variation of No. 10 is due to stellar rotation, this would be the first discovery of stellar rotation from a protostar. On the other hand, the variability can also be understood as an X-ray flare without any significant spectral variation. In this case, the exponential decay time and emitted energy are estimated to be 4×10^4 s and 2×10^{35} erg, respectively. We should be conservative until future long-term X-ray and infrared monitoring can be obtained.

No. C3

In the error region of C3, we found 2 candidates, EL 23 (Elias 1978; Andre, Montmerle 1994; Vrba et al. 1975) and GY 29 (Greene, Young 1992). ROSAT also found this source to be a candidate of EL 23 with a finer spatial resolution, like ROXR 1–25 (Casanova et al. 1995). Hence, source C3 is likely to be associated with ROXR 1-25 and EL 23 = S2.

No. C5

This source is found to exhibit the largest hardness ratio (5–7 keV/2–5 keV) among the observed X-ray sources. Allowing a reasonable temperature range of 2–3 keV, we estimated from the hardness ratio the $N_{\rm H}$ value to be $(2\text{–}3) \times 10^{23}$. In spite of this possible large absorption, no class-I source was found in the error region; instead, class-II sources WL 17 and GY 201 were found. Further details concerning the X-rays were not available, mainly due to large contamination from a nearby bright X-ray source, EL 29.

No. C7

This source shows a flare event only in the hard X-ray band, which indicates that either the spectrum becomes hard, or the absorption becomes larger during a flare.

4. Conclusion

We have studied images, spectra and temporal variations in the 0.5–10 keV energy band of the ρ Oph members using data obtained by the X-ray astronomy satellite ASCA.

1. Using 3 energy bands and time-divided X-ray images, we found 19 X-ray sources in the ρ Oph region and resolved a previously identified X-ray source (No. 9) into two sources (9A and 9B). Eight among the 19 sources are new X-ray sources which have not been catalogued by either Einstein or ROSAT observations.

2. We found no X-rays from the class-0 source VLA 1623, but did discover hard and variable X-rays from two class-Is (EL 29 and WL 6) and one possible candidate (WLY 2-46) near to the cluster core.

3. A large absorption of $N_{\rm H} = 2 \times 10^{23}$ cm^{-2} was found from the class-I source EL 29 during its flare. We infer that large amounts of circumstellar materials have an anisotropic distribution, such as a protostellar disk around the central source, which increases the line-of-sight X-ray absorption.

4. We found a hint that the X-ray modulation of the source No. 10 (WL 6) is due to its stellar rotation with about a 0.97-d period with a large X-ray bright spot covering 30% of the stellar surface.

5. Flare parameters observed from 5 X-ray sources are similar to solar flares, except for their X-ray luminosities or loop sizes. The loop sizes are comparable to the solar diameter, and the magnetic field in the X-ray emitting region is estimated to be 200–400 G.

The authors thank all the members of the ASCA team, particularly those who took great efforts in the software and hardware development and support daily operation of ASCA. The authors also appreciate the useful comments and advice of Drs. E. Feigelson, Y. Tawara, S. Sato, K. Leighly, A. Mizuno, S. Matsuura, T. Hirao, and K. Tachihara.

References

Adams F.C., Lada C.J., Shu F.H. 1987, ApJ 312, 788
Andre P., Montmerle T. 1994, ApJ 420, 837
Andre P., Montmerle T., Feigelson E.D. 1987, AJ 93, 1182
Antunes A., Nagase F., White N.E. 1994, ApJ 436, L83
Barsony M., Burton M.G., Russell A.P.G., Carlstrom J.E., Garden R. 1989, ApJ 346, L93
Bouvier J., Appenzeller I. 1992, A&AS 92, 481
Brown R.L., Zuckerman B. 1975, ApJ 202, L125
Burke B.E., Mountain R.W., Harrison D.C., Bautz M.W., Doty J.P., Ricker G.R., Daniels P.J. 1991, IEEE Trans ED-38, 1069
Casanova S., Montmerle T., Feigelson E.D., Andre P. 1995, ApJ 439, 752
Chini R. 1981, A&A 99, 346
Comeron F., Rieke G.H., Burrows A., Rieke M.J. 1993, ApJ 416, 185
Dame T.M., Ungerechts H., Cohen R.S., Geus E.J., Grenier I.A., May J., Murphy D.C., Nyman L.A. et al. 1987, ApJ 322, 706
Dolidze M.V., Arakelyan M.A. 1959, SvA 3, 434
Drake S.A., Singh K.P., White N.E., Simon T. 1994, ApJ 436, L87
Elias J.H. 1978, ApJ 224, 453
Feldman U. 1992, Phys. Scr. 46, 202
Gorenstein P. 1975, ApJ 198, 95
Grasdalen G.L., Strom K.M., Strom S.E. 1973, ApJ 184, L53
Greene T.P., Wilking B.A., Andre P., Young E.T., Lada C.J. 1994, ApJ 434, 514
Greene T.P., Young E.T. 1992, ApJ 395, 516
Grosso N., Montmerle T., Feigelson E.D., Andre P., Casanova S., Gregorio-Hetem J. 1997, Nature submitted
Hanner M.S., Brooke T.Y., Tokunaga A.T. 1995, ApJ 438, 250
Haro G. 1949, AJ 54, 188
Hartmann L.W., Soderblom D.R., Stauffer J.R. 1987, AJ 93, 907
Herbig G.H., Bell K.R. 1988, Lick Obs. Bull. No. 1111
Kenyon S.J., Calvet N., Hartmann L. 1993a, ApJ 414, 676
Kenyon S.J., Whitney B.A., Gomez M., Hartmann L. 1993b, ApJ 414, 773
Koyama K. 1987, PASJ 39, 245
Koyama K., Asaoka I., Kuriyama T., Tawara Y. 1992, PASJ 44, L255
Koyama K., Hamaguchi K., Ueno S., Kobayashi N., Feigelson E.D. 1996, PASJ 48, L87
Koyama K., Maeda Y., Ozaki M., Ueno S., Kamata Y., Tawara Y., Skinner S., Yamauchi S. 1994, PASJ 46, L125 (Paper I)
Kukarkin B.V., Kholopov P.N., Artiukhina N.M., Fedorovich V.P., Frolov M.S., Goranskij V.P., Gorynya N.A., Karitskaya E.A. et al. 1981, New Catalogue of Suspected Variable Stars (Nauka, Moscow)
Leous J.A., Feigelson E.D., Andre P., Montmerle T. 1991, ApJ 379, 683
Loren R.B., Sandqvist A., Wootten A. 1983, ApJ 270, 620
Merrill P.W., Burwell C.G. 1950, ApJ 112, 72
Montmerle T., Koch-Miramond L., Falgarone E., Grindlay J.E. 1983, ApJ 269, 182
Morrison R., McCammon D. 1983, ApJ 270, 119
Ohashi T., Ebisawa K., Fukazawa Y., Hiyoshi K., Horii M., Ikebe Y., Ikeda H., Inoue H. et al. 1996, PASJ 48, 157
Raymond J.C., Smith B.W. 1977, ApJS 35, 419
Rosner R., Golub L., Vaiana G.S. 1985, ARA&A 23, 413
Ryter C.E. 1996, Ap&SS 236, 285
Ryter C.E., Cesarsky C.J., Audouze J. 1975, ApJ 198, 103
Savage B.D., Mathis J.S. 1979, ARA&A 17, 73
Schlickeiser R., Harwit M., Ozel M.E., Sieber W., Younis S.M., Schinckel A. 1989, A&A 216, 197
Serlemitsos P.J., Jalota L., Soong Y., Kunieda H., Tawara Y., Tsusaka Y., Suzuki H., Sakima Y. et al. 1995, PASJ 47, 105
Shu F.H., Adams F.C., Lizano S. 1987, ARA&A 25, 23
Simon M., Howell R.R., Longmore A.J., Wilking B.A., Peterson D.M., Chen W.P. 1987, ApJ 320, 344
Sofia U.J., Cardelli J.A., Savage B.D. 1994, ApJ 430, 650
Stine P.C., Feigelson E.D., Andre P., Montmerle T. 1988, AJ 96, 1394
Strom K.M., Kepner J., Strom S.E. 1995, ApJ 438, 813
Struve O., Rudkjøbing M. 1945, ApJ 109, 92
Tanaka Y., Inoue H., Holt S.S. 1994, PASJ 46, L37
Thome J.M. 1892, Resultados del Observatorio Nacional Argentino, 16, 1
Tsusaka Y., Suzuki H., Yamashita K., Kunieda H., Tawara Y., Ogasaka Y., Uchibori Y., Honda H. 1995, Appl. Opt. 34, 4848
van den Oord G.H.J., Mewe R., Brinkman A.C. 1988, A&A 205, 181
Vrba F.J., Strom S.E., Strom K.M. 1976, AJ 81, 958
Vrba F.J., Strom K.M., Strom S.E., Grasdalen G.L. 1975, ApJ 197, 77
Wilking B.A. 1989, PASP 101, 229
Wilking B.A., Lada C.J. 1983, ApJ 274, 698
Wilking B.A, Schwartz R.D., Blackwell J.H. 1987, AJ 94, 106
Wilking B.A., Lada C.J., Young E.T. 1989, ApJ 340, 823

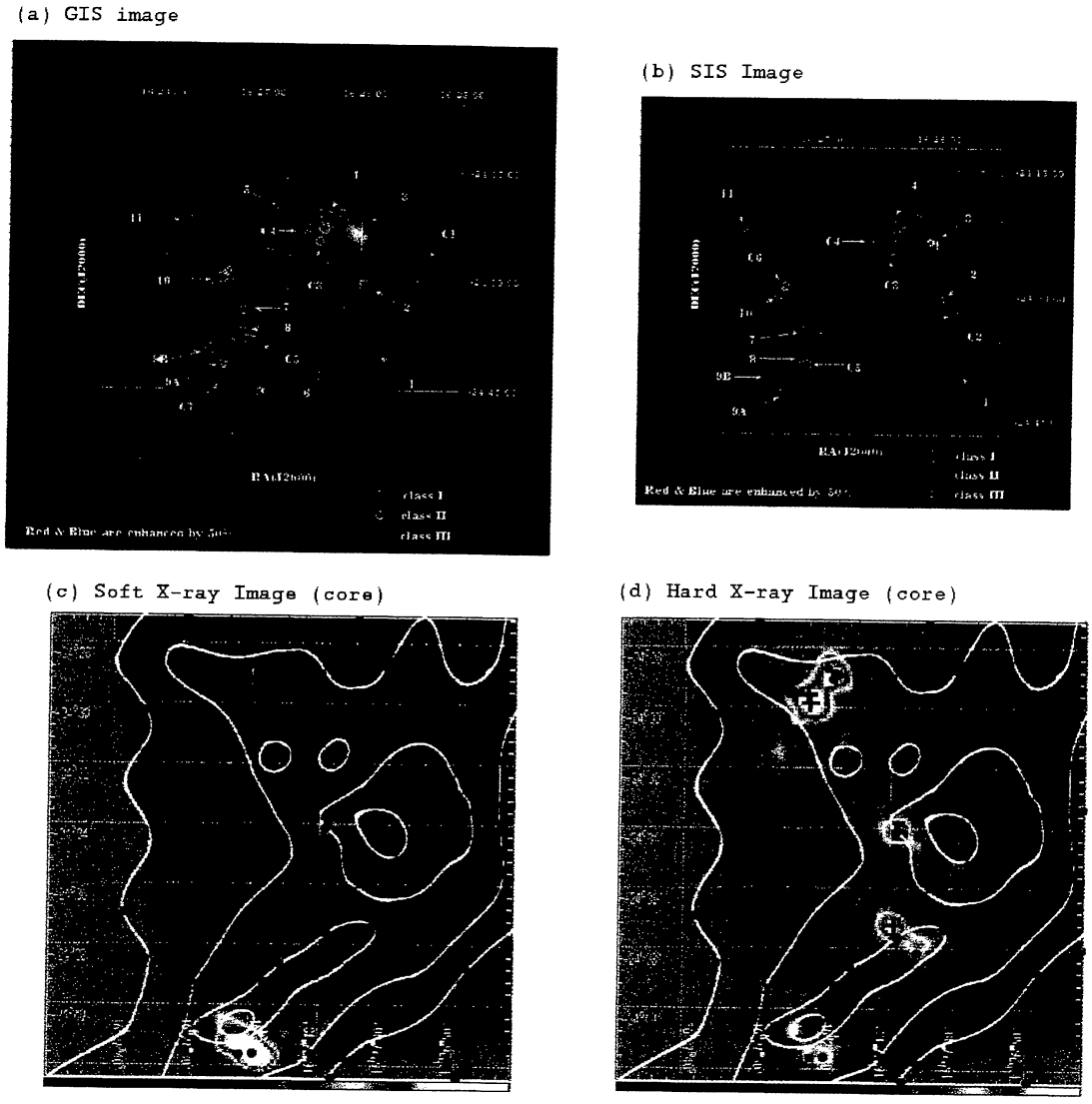

Fig. 1. ASCA images of the ρ Oph cloud core, main body. The upper two images are normalized RGB-weighted images of GIS 2+GIS 3 and SIS 0+SIS 1 (ab), respectively. Red, green, and blue correspond to 5–7 keV, 2–5 keV, and 1–2 keV flux, respectively (red and blue are enhanced by 50% to make reddened objects clear). The open circles show the cluster members and IR classes (Andre, Montmerle 1994) and pointing arrows show ROXA sequential numbers. The lower two images (cd) are SIS 0+SIS 1 images in the 0.5–2 and 2–10 keV energy bands. The contours are the $C^{18}O(1\rightarrow0)$ column densities (Wilking, Lada 1983), in units of $10^{16}cm^{-2}$, from 1.0 to 2.5 in steps of 0.5, correponding to $A_V \sim 30$, 50, 70, 100, respectively. IR sources from Greene and Young (1992) are indicated by the closed circle; the crosses are class-I sources.